Non-spatial hippocampal behavioral timescale synaptic plasticity during working memory is gated by entorhinal inputs

Conor C. Dorian[1], Jiannis Taxidis[2,3], Peyman Golshani[1,4,5,6,7,*]

[1]Department of Neurology, David Geffen School of Medicine, University of California Los Angeles, Los Angeles, CA, USA.
[2]Program in Neurosciences and Mental Health, Hospital for Sick Children, Toronto, Ontario, Canada.
[3]Department of Physiology, University of Toronto, Toronto, Ontario, Canada.
[4]Greater Los Angeles Veteran Affairs Medical Center, Los Angeles, CA, USA.
[5]Intellectual and Developmental Disabilities Research Center, University of California Los Angeles, Los Angeles, CA, USA.
[6]Semel Institute for Neuroscience and Human Behavior, University of California, Los Angeles, CA, USA.
[7]Integrative Center for Learning and Memory, University of California, Los Angeles, CA, USA.

* Corresponding author: pgolshani@mednet.ucla.edu

ABSTRACT

Behavioral timescale synaptic plasticity (BTSP) is a form of synaptic potentiation where the occurrence of a single large plateau potential in CA1 hippocampal neurons leads to the formation of reliable place fields during spatial learning tasks. We asked whether BTSP could also be a plasticity mechanism for generation of non-spatial responses in the hippocampus and what roles the medial and lateral entorhinal cortex (MEC and LEC) play in driving non-spatial BTSP. By performing simultaneous calcium imaging of dorsal CA1 neurons and chemogenetic inhibition of LEC or MEC while mice performed an olfactory working memory task, we discovered BTSP-like events which formed stable odor-specific fields. Critically, the success rate of calcium events generating a significant odor-field increased with event amplitude, and large events exhibited asymmetrical formation with the newly formed odor-fields preceding the timepoint of their induction event. We found that MEC and LEC play distinct roles in modulating BTSP: MEC inhibition reduced the frequency of large calcium events, while LEC inhibition reduced the success rate of odor-field generation. Using two-photon calcium imaging of LEC and MEC temporammonic axons projecting to CA1, we found that LEC projections to CA1 were strongly odor selective even early in task learning, while MEC projection odor-selectivity increased with task learning but remained weaker than LEC. Finally, we found that LEC and MEC inhibition both slowed representational drift of odor representations in CA1 across 48 hours. Altogether, odor-specific information from LEC and strong odor-timed activity from MEC are crucial for driving BTSP in CA1, which is a synaptic plasticity mechanism for generation of both spatial and non-spatial responses in the hippocampus that may play a role in explaining representational drift and one-shot learning of non-spatial information.

INTRODUCTION

In many situations, learning is not a gradual process. In fact, our ability to make associations after a single experience is critical for survival. While there have been dramatic improvements in artificial intelligence and machine learning algorithms that implement 'one-shot learning' [1, 2], the neural underpinnings of this abrupt form of learning have remained elusive. In the hippocampus, a region recognized for its importance in learning and memory, behavioral timescale synaptic plasticity (BTSP) has emerged as a robust mechanism for the rapid generation of spatial representations (place fields) following the occurrence of plateau potentials [3, 4, 5, 6, 7, 8, 9, 10]. However, the hippocampus not only represents the location of animals in space [11, 12, 13, 14], but also non-spatial sensory information [15, 16, 17, 18]. The hippocampus dynamically links these sensory experiences across time through sequential firing that tracks the passage of time after specific events [13, 18, 19, 20, 21]. It is unclear whether BTSP also drives the formation of non-spatial sensory-driven or internally generated hippocampal representations, which can form the basis for 'one-shot learning'.

Hebbian plasticity mechanisms such as spike-timing dependent plasticity require causality and many repetitions to potentiate synapses when presynaptic spikes precede postsynaptic action potentials by a few milliseconds [22, 23, 24, 25]. While this mechanism may play a role in modulating hippocampal responses, BTSP on the other hand, has many features which could make it a more robust and rapid mechanism for the generation of non-spatial receptive fields. During spatial learning tasks, a single calcium plateau potential can serve as the induction event, asymmetrically boosting synaptic inputs that occur several seconds before the induction event, leading to a membrane potential ramp and reliable spatial firing on subsequent trials [4, 7, 8]. It is not known whether plateau potentials occurring during non-spatial tasks could also boost synaptic inputs at specific time points in the task leading to the rapid formation of stable representations of sensory stimuli, time, and reward/outcome. The rapid induction of these non-spatial hippocampal representations by BTSP could form the basis for rapid learning in the hippocampus.

The role of the entorhinal cortex (EC) in inducing BTSP events [9] and relaying sensory information during non-spatial tasks [17, 26, 27] is poorly understood. CA1 receives direct layer III EC input via the temporammonic (TA) pathway and indirect input via the perforant path from layer II EC to dentate gyrus, which then projects to CA3, which in turn projects to CA1 [28, 29]. Lateral and medial EC (LEC and MEC) have distinct inputs and behaviorally relevant response properties: LEC robustly represents olfactory information [30, 31, 32, 33], while MEC is more recognized for its encoding of visuo-spatial information [34, 35, 36, 37]. Furthermore, the MEC plays a major role in the induction of plateau potential 'teaching signals' during BTSP induced during spatial learning tasks [9]. Yet, whether MEC and LEC play a differential role in the generation of BTSP during non-spatial tasks remains to be determined.

To address these questions, we investigated multimodal representations within CA1 and EC during a non-spatial olfactory delayed non-match-to-sample (DNMS) working memory task [18]. We have previously shown that CA1 pyramidal neurons fire sequentially in response to specific odors and across the 5-second delay period during DNMS performance [18]. We hypothesized that non-spatial BTSP can generate odor representations in CA1 and that this process would be modulated by MEC and LEC inputs. Using two-photon calcium imaging of dorsal CA1, we recorded non-spatial 'BTSP-like' events that formed odor-specific fields in CA1 during expert performance of the DNMS task. Through simultaneous chemogenetic inhibition of LEC or MEC and calcium imaging of CA1, we investigated the role of each EC region in driving odor-specific 'BTSP-like' events. We found that MEC inhibition decreased the frequency of large calcium induction events, while LEC inhibition reduced the success rate of odor-field generation. Additionally, we performed two-photon calcium imaging of LEC and MEC

axons in the TA pathway projecting onto dorsal CA1 during learning of the task to investigate how EC inputs to CA1 change with experience and improved performance. Altogether, we demonstrate that MEC's strong firing to odor presentations drives large plateau-like calcium events in CA1, and LEC's odor-selectivity mediates plasticity in the formation of odor-fields after the large calcium induction event.

RESULTS

We used *in-vivo* two-photon calcium imaging to record the activity of neurons in the pyramidal layer of dorsal CA1 while animals performed an olfactory delayed non-match-to-sample (DNMS) working memory task (Figure 1 A-E). Adult male and female mice (n=17) were injected with AAV1-Syn-jGCaMP8f into the right dorsal CA1 and implanted with a 3mm diameter glass-bottomed titanium cannula above the intact alveus after aspiration of the overlying cortex and corpus callosum [18] (Figure 1 E). After one week of recovery, mice were water-deprived and trained on the olfactory DNMS working memory task [18, 38], while head-fixed on a spherical treadmill (Figure 1 A-B). Each trial consisted of two 1-second odor presentations separated by a 5-second delay period. One second after the offset of the 2nd odor, there was a 3-second reward period during which the choice of the animal was determined. Mice were trained to lick the lickport to release water during this reward period if the two odors did not match (correct 'hit'). Mice learned to refrain from licking the lickport if the odors matched (correct 'rejection'), and overall performance was quantified as the percentage of correct 'hits' and correct 'rejections' out of all trials (Figure 1 C). We considered performance above 85% to be expert level. Each session of the DNMS task consisted of 5 blocks of 20 trials, with pseudorandomly distributed odor combinations (Figure 1 D). Mice were recorded for 8 days during expert performance for a total of 136 recording sessions yielding an average of 312 $\pm$ 125 (mean $\pm$ standard deviation) active neurons per day. We successfully imaged the same field of view (FOV) for each of the 8 days for all animals. Calcium signals were extracted and deconvolved using Suite2p [39] (see methods).

Non-spatial BTSP-like events in CA1 formed stable odor-specific fields

In our previous work, we found that a population of hippocampal neurons fired during specific epochs of the DNMS task [18]. CA1 pyramidal neurons fired during the presentation of specific odors or at time points during the delay period after presentation of specific odors [18]. Here, we observed CA1 neurons with activity patterns consistent with BTSP during expert DNMS performance (Figure 1 G-H and Figures S1-S3). Namely, neurons without a clear odor or time-field developed a stable field after a single spontaneous large calcium event as the induction event (putative plateau potential). To quantify these rare events, we developed strict criteria for a single calcium event to be considered an 'induction event' that could potentially generate an odor-field (see methods).

With increasing 'induction event' amplitude, success rate for induction of an odor-field increased (Figure 1 I), strongly suggesting a causal role for these induction events in driving the formation of odor-fields. We also found that only events larger than 10 STD exhibited a significantly asymmetrical formation with the newly formed odor-fields preceding the timepoint of their induction event, (Figure 1 K) suggesting that these subset of induction events were true BTSP events. Based on these findings, we set the criteria for an 'induction event' to be considered a 'plateau-like' event to be that the large calcium induction event must have an amplitude greater than 10 STD. For these 'plateau-like' events, nearly all of the successful induction events peaked during the odor presentation or immediately after the offset, with the success rate reaching 15% during the second half of the odor presentation period (Figure 1 J). We observed only 26 events (8% of the 323 successful events) yielding time-fields beyond 0.5 seconds after odor offset, and only 24 events yielding reward-related fields in separate analysis

(Figure S3). The newly formed odor-specific fields peaked at 0.42 $\pm$ 0.14 seconds prior to the onset of the putative plateau potential (n=323 successful 'plateau-like' events) (Figure 1 L). The small events that represented the random chance of an event passing our strict criteria had a success rate that only peaked at 0.6% during odor presentation, and they did not have significant asymmetrical formation (Figure S4 A-B).

To determine if motor movements of the animal influenced non-spatial BTSP events, we recorded the movements of the spherical Styrofoam treadmill during performance of the task (Figure S4 C). Mice exhibited a range of movement patterns while performing the task with some mice rarely moving on the treadmill and many mice primarily flinching or twitching at the onset of odor presentations (Figure S4 C). However, nearly all mice had bouts of running that we defined as periods of continuous locomotion for greater than 2 seconds. As expected, the frequency of low amplitude calcium events was greater during periods of running (1.83 $\pm$ 0.21 small events per neuron per minute during non-running periods compared to 3.31 $\pm$ 0.68 small events per neuron per minute during running bouts) (Figure S4 F). Additionally, running increased the rate of 'plateau-like' events (0.012 $\pm$ 0.005 'plateau-like' events per neuron per minute during non-running periods compared to 0.028 $\pm$ 0.010 'plateau-like' events per neuron per minute during running bouts) (Figure S4 G). However, running during the 'plateau-like' event did not impact the success rate of formation of an odor-field (2.07 $\pm$ 1.25 % success rate following 'plateau-like' event during non-during periods compared to 2.00 $\pm$ 2.63 % success rate during running bouts) (Figure S4 H). Therefore, running increased the rate of 'plateau-like' events but not the formation of odor-fields, which suggests that the 'BTSP-like' events we observed are non-spatial in nature. Together these findings suggest that BTSP can generate non-spatial hippocampal representations.

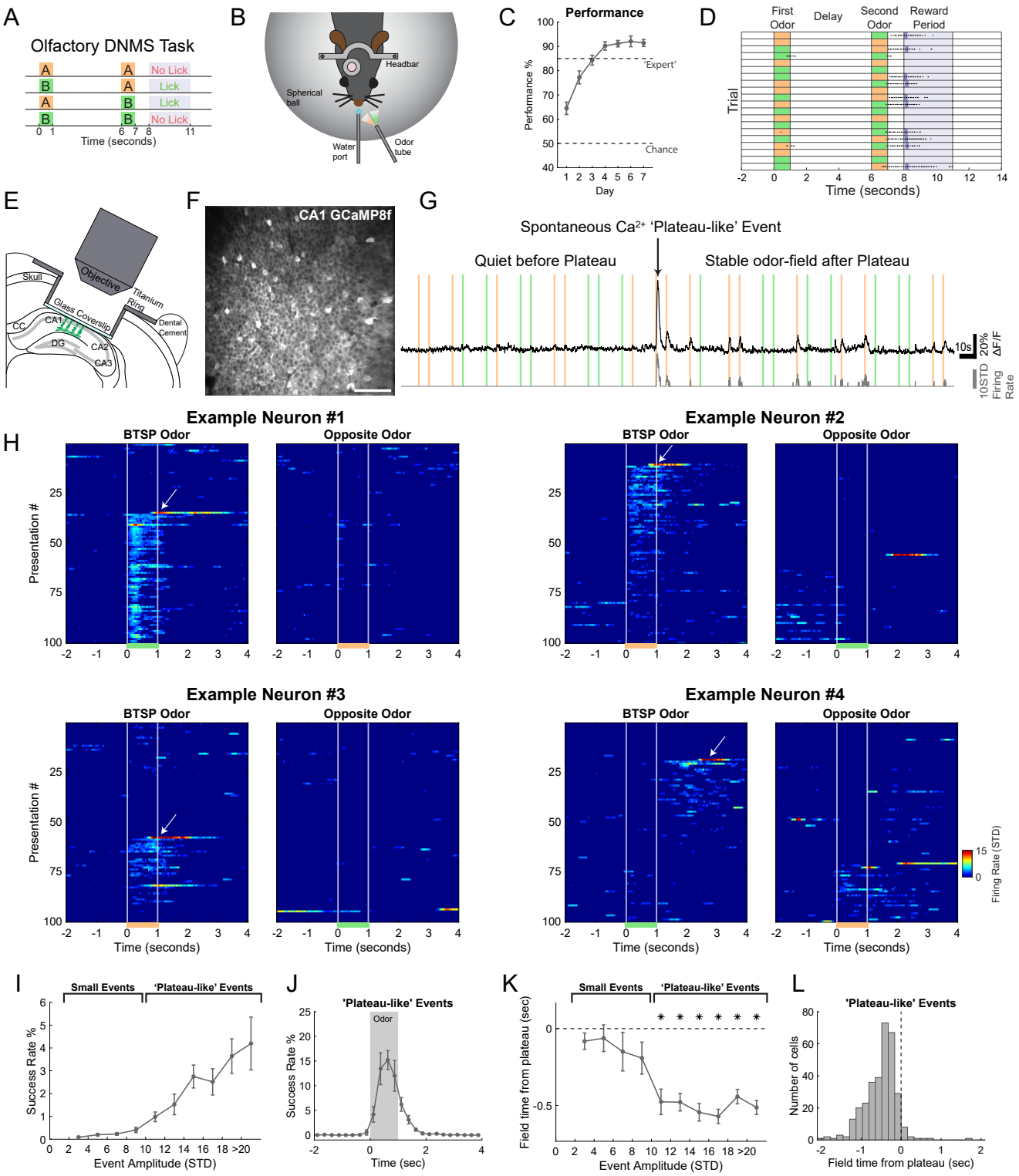
A
Olfactory DNMS Task
No Lick
Lick
Lick
No Lick
Time (seconds)
B
Headbar
Spherical ball
Water port
Odor tube
C
Performance
Performance %
'Expert'
Chance
Day
D
First Odor
Delay
Second Odor
Reward Period
Trial
Time (seconds)
E
Skull
Objective
Titanium Ring
Glass Coverslip
Dental Cement
CC
CA1
DG
CA2
CA3
F
CA1 GCaMP8f
G
Spontaneous Ca2+ 'Plateau-like' Event
Quiet before Plateau
Stable odor-field after Plateau
10s
20% ΔF/F
10STD Firing Rate
H
Example Neuron #1
Example Neuron #2
Example Neuron #3
Example Neuron #4
BTSP Odor
Opposite Odor
Presentation #
Time (seconds)
Firing Rate (STD)
I
Small Events
'Plateau-like' Events
Success Rate %
Event Amplitude (STD)
J
'Plateau-like' Events
Odor
Success Rate %
Time (sec)
K
Small Events
'Plateau-like' Events
Field time from plateau (sec)
Event Amplitude (STD)
L
'Plateau-like' Events
Number of cells
Field time from plateau (sec)

Figure 1: Behavioral timescale synaptic plasticity (BTSP) events in a non-spatial working memory task. **A)** Schematic of the olfactory delayed non-match-to-sample (DNMS) task. Water delivery and licking behavior was assessed during the 3-second reward period. **B)** Mice were head-fixed above a Styrofoam spherical ball to allow running. **C)** Behavioral performance across 7 days of learning (n=33). Chance level performance was 50%, and we considered 85% to be 'expert' performance. **D)** Example block of perfect performance for 20 trials. Dots indicate licks and dark blue bars indicate water delivery. **E)** Schematic of two-photon calcium imaging of dorsal CA1 pyramidal neurons. **F)** Example field of view of CA1 neurons expressing GCaMP8f. Scale bar is 100µm. **G)** Example trace of one neuron with a 'BTSP-like' event and odor-field formed. Colored bars indicate odor presentations. Black trace is $\Delta F/F$, and gray is z-scored deconvolved signal. **H)** Four examples of 'BTSP-like' events. White vertical lines indicate odor onset and offset, and white arrows point to spontaneous induction 'plateau-like' events. **I)** Success rate of a calcium event generating an odor-field increases with induction-event amplitude. Success rate is defined as percentage of events that generate a significant odor-field. Standard error bars represent the standard error of the mean across the 17 animals. Events above 10 STD are considered 'plateau-like' events. **J)** Success rate is highest during odor presentation (for only 'plateau-like' events). **K)** Asymmetrical field formation with trial time difference between 'plateau-like' event peak and formed odor-field peak. This difference is only significant for 'plateau-like' events. Thus, the 'small events' represent chance events that passed our criteria and were likely not BTSP. **L)** Histogram showing asymmetrical distribution for all 323 successful 'plateau-like' events.

Chemogenetic inhibition of entorhinal cortex disrupted non-spatial BTSP

Entorhinal inputs can drive BTSP induction events during spatial learning tasks [9, 40]. To determine whether entorhinal inputs may also play a role in the generation of 'plateau-like' events during non-spatial BTSP, we used a chemogenetic strategy to inhibit lateral entorhinal cortex (LEC) or medial entorhinal cortex (MEC), while imaging CA1 calcium activity during the working memory task. Mice were injected with AAV1-Syn-jGCaMP8f in the dorsal CA1 and were subsequently implanted with an optical canula over CA1 as in the previous section. These mice also underwent injection of AAV5-CaMKII-PSAM4 into either LEC (n=6 mice) or MEC (n=5 mice) to express the potent chemogenetic inhibitor PSAM4 [41] in excitatory neurons of either structure. Control mice underwent injections of AAV5-CaMKII-mCherry into either LEC (n=3 mice) or MEC (n=3 mice). Animals were water-deprived, trained on the task, and imaged 3 weeks after viral expression. Each animal was recorded for 8 days after reaching expert level performance. Between 10-20 minutes before two-photon calcium imaging began each day, mice received an intraperitoneal (IP) injection of saline or uPSEM (the effector molecule for PSAM4). Saline and uPSEM injections were alternated daily and animals were counter-balanced such that half of the mice received injections of uPSEM on the first day and the other half of mice received injections of saline. We compared the activity of matched neurons over 4 pairs of days, where animals received saline on one day and uPSEM on the other day.

Despite a lack of a behavioral effect with LEC or MEC inhibition (Figure S5), both strongly affected non-spatial 'BTSP-like' events. MEC inhibition significantly reduced the number of 'plateau-like' events from 1.91 $\pm$ 0.95 per neuron per day to 1.60 $\pm$ 1.09 per neuron per day (Figure 2 B). In contrast, LEC did not affect the number of 'plateau-like' events, but dramatically reduced the success rate of 'plateau-like' events in inducing a new odor-field from 2.13 $\pm$ 2.44% to 0.89 $\pm$ 1.32%, while MEC inhibition did not significantly alter the success-rate (Figure 2 C). Importantly, neither LEC nor MEC inhibition affected locomotion or the percentage of time spent running, so these effects could not be explained by differences in animal movement (Figure S5 B-C). Together, these findings suggest that MEC affects the generation of large 'plateau-like' events in CA1, while LEC activity increases the likelihood that these events result in successful field generation.

LEC inhibition reduced strength of odor representations in dorsal CA1, while MEC inhibition increased strength

Given that LEC inputs have been previously shown to encode odor-related information [30, 31, 32, 33], we hypothesized that they could convey odor-related information to CA1 in our DNMS task. If so, we would expect inhibition of LEC but not MEC to decrease odor-selectivity in CA1, potentially driving the decrease in success rate of 'plateau-like' events in generating odor-fields. Indeed, LEC chemogenetic inhibition significantly decreased odor-selectivity values and the percentage of odor-selective neurons (Figure 2 D and Figure S6 A). None of the 6 mCherry controls animals showed a shift in odor-selectivity (Wilcoxon signed-rank test pairing all neurons, $p > 0.05$ for each animal). First and second odor-selectivity were similarly modulated (Figure S6 B). The proportion of significantly odor-selective neurons (based on comparisons with shuffled controls; see methods) was 24.5 $\pm$ 10.7% on saline control days and only 16.2 $\pm$ 10.9% on uPSEM inhibition days in LEC experimental PSAM4 animals. In contrast, MEC inhibition showed a small change in the opposite direction with 20.7 $\pm$ 5.8% of neurons being odor selective on saline control days and 21.8 $\pm$ 5.5% on uPSEM inhibition days in MEC experimental PSAM4 animals. Therefore, LEC inhibition weakened CA1 neuron odor-selectivity.

To further confirm this effect, we performed binary support vector machine (SVM) decoding training and testing on the same day to evaluate the relative strength of odor encoding on saline days compared to uPSEM days. Overall, LEC inhibition significantly decreased odor decoding accuracy, while MEC

inhibition significantly improved odor decoding (Figure 2 E-F). During the odor presentation period (subsampling only 100 neurons), the decoding accuracy in LEC experimental PSAM4 animals was 76.4 $\pm$ 11.0% on saline control days and decreased to 66.7 $\pm$ 13.9% on uPSEM inhibition days. In contrast, MEC experimental PSAM4 mice had a decoding accuracy of 79.0 $\pm$ 5.8% on saline control days, which increased to 82.5 $\pm$ 5.5% on uPSEM inhibition days. Odor decoding of control animals expressing mCherry was unaffected by uPSEM administration (Figure S6 A-B). MEC inhibition only increased decoding accuracy during odor presentation, while LEC inhibition decreased odor decoding accuracy during the earlier part of the delay period as well (Figure 2 E). Increasing the number of subsampled neurons for decoding led to improvements in odor decoding, but in general differences between MEC and LEC inhibition were observed for a large range of neuron numbers subsampled for decoding analysis (Figure S6 D).

Collectively, LEC inhibition strongly decreased, whereas MEC inhibition modestly increased odor-selectivity and decodability in CA1. The reduction of odor-selectivity by LEC inhibition may have driven the reduction in the success rate of ‘plateau-like’ events in generating odor-fields, though additional mechanisms could potentially contribute to this effect.

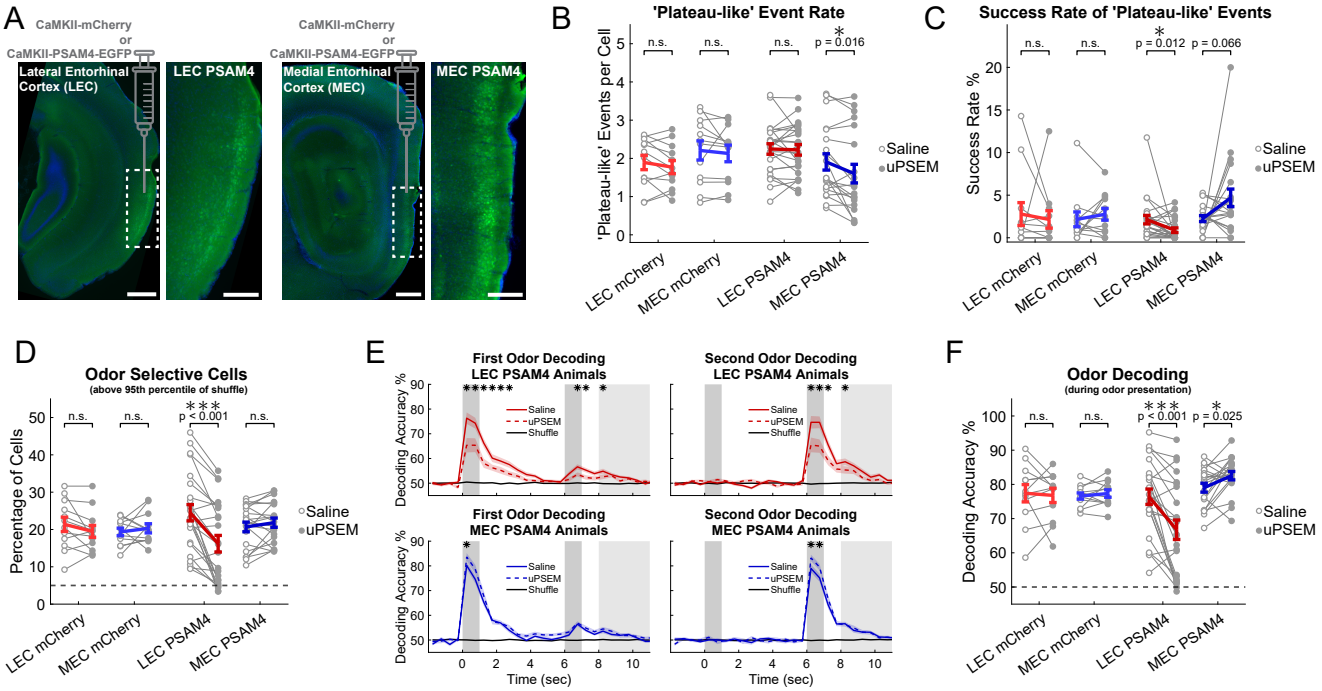

Figure 2: LEC and MEC inhibition differentially modulated BTSP, and LEC inhibition weakened odor-selectivity in CA1. **A)** Injections of virus to drive the expression of mCherry or PSAM4 were delivered to either LEC or MEC. Images showing LEC are from coronal sections, while MEC are from sagittal sections. For both LEC and MEC, the larger image on the left has a 500µm scale bar and the right image is a zoom of the white outline with a 200µm scale bar. **B)** Number of events greater than 10 STD per neuron per day. Paired dots represent the pairs of imaging days (4 per animal). Statistics are two-way ANOVA (animal and pair) with repeated measures on the saline/uPSEM condition. **C)** Success rate of 'plateau-like' events generating an odor-field. **D)** Percentage of neurons that had a selectivity value above 95th percentile of shuffle. Statistics are also two-way ANOVA (animal and pair) with repeated measures on the saline/uPSEM condition. **E)** Binary support vector machine (SVM) decoding of first and second odor across the trial structure with 0.5 second bins for experimental animal groups (repetitive subsampling of 100 neurons for each recording session). Thinner gray bars indicate odor presentation and wider bar from seconds 8-11 is the reward period. Statistics are the same, and asterisks indicate bins with $p < 0.05$ (corrected for multiple comparisons using the Benjamini-Hochberg procedure). **F)** Odor decoding performance only during the odor presentation period.

Two-photon calcium imaging of entorhinal cortical axons in dorsal CA1 revealed differential sequential activity in LEC and MEC inputs

The EC is the primary cortical input to the hippocampus; CA1 receives direct layer III EC input via the temporammonic (TA) pathway and indirect input via the perforant path from layer II EC to dentate gyrus, which then projects to CA3, which in turn projects to CA1 [28, 29]. Given the contribution of MEC in driving 'plateau-like' events, we asked if there are differences in timing of LEC and MEC TA inputs. Also, given the strong differences in odor decodability observed in dorsal CA1 with LEC versus MEC inhibition, we asked whether TA inputs from LEC and MEC differ in the sensory and task-related information they convey to CA1. Do LEC and MEC TA inputs change as mice learn the task?

To address these questions, we performed two-photon calcium imaging of LEC or MEC TA axons in dorsal CA1 as mice learned the DNMS task. Adult male and female mice were injected with AAV1-CaMKII-Cre and AAV1-CAG-FLEX-jGCaMP7s in either LEC (n=8) or MEC (n=8) (Figure 3 A and C). Mice were implanted with hippocampal windows as in the previous experiments. After 3 weeks of expression, confocal imaging demonstrated extensive GCaMP7s axonal expression of TA inputs within the stratum lacunosum-moleculare (SLM) layer, as well as layer II EC perforant path axons ramifying deeper within the stratum moleculare (MOL) layer of the dentate gyrus. *In-vivo*, we could selectively image TA EC axons 300 and 400µm beneath the alveus. Post-hoc histology after two-photon imaging experiments also confirmed that all mice had extensive expression of GCaMP7s in axons within the SLM layer of hippocampus and somatic expression restricted to either LEC or MEC. In these experiments, imaging experiments began on the first day of training when mice are presented with matched pairs and began learning to refrain from licking on these trials (see methods). Recordings were processed with Suite2p [39] using parameters optimized for axonal imaging, followed by post hoc fusion of axon segments with highly correlated activity which were branches of the same axon (see methods) (Figure 3 B and D).

In trained animals, a proportion of LEC and MEC TA axons responded reliably to different task variables. Some axons had responses which had significant peaks during the odor presentation, some during odor offset, and others during the delay period (Figure 3 E and F). Altogether, the LEC or MEC axonal populations had sequential activity that tiled the entire first odor presentation and delay period. However, these sequences differed drastically between LEC and MEC; a much higher proportion of MEC axons had significant peaks during odor presentations compared to LEC axons (Figure 3 G-J).

To investigate how LEC and MEC inputs to CA1 change with learning, we first visualized the sequential firing of significantly modulated axons (see methods) during expert performance and below expert performance (Figure 3 G). We noticed stark differences in the proportion of axons with peak activity during the odor compared to during the delay between LEC and MEC. There were also clear differences in these proportions when comparing poor performance to expert performance. During days of expert performance, MEC had more axons with peak firing during odor presentation compared to LEC (26.9 $\pm$ 8.7% compared to 10.1 $\pm$ 7.2%, ANOVA $p < 0.001$), while LEC had more axons with peak firing during the delay period compared to MEC (5.9 $\pm$ 1.9% compared to 2.5 $\pm$ 1.1%, ANOVA $p < 0.001$) (Figure 3 I). As a result, MEC axons also showed greater trial reliability as compared to LEC (Figure S7 C). The percentage of MEC axons with peak firing during odor presentation increased across learning (Pearson's $r = 0.311$), while those with peak firing during the delay period decreased (Pearson's $r = -0.433$). Meanwhile, the proportion of LEC axons with peak firing during odor and delay periods remained stable with learning (Pearson's $r = 0.082$ and 0.074).

In summary, timing of LEC inputs to CA1 were stable with learning, while MEC inputs became more tuned to the odor presentation period. Given that MEC inhibition reduced the rate of 'plateau-like'

events in CA1, we hypothesize that this strong MEC input timed to the odor presentation is likely key for driving 'plateau-like' events.

LEC odor representations were stable during learning, while MEC tuned firing to odor presentation and odor-selectivity emerged

Although a higher proportion of MEC axons were tuned to firing during the odor presentation, examination of sequential firing patterns suggested that these axons were firing with less odor-specificity (Figure 3 G-H and Figure S7 A-B). To quantify odor information carried by EC axons, we calculated odor-selectivity and odor decoding accuracy. Despite the increased number of MEC axons with peak firing during the odor presentation, LEC had a greater proportion of significantly odor-selective axons (14.3 $\pm$ 6.8% in LEC and 10.3 $\pm$ 4.6% in MEC, ANOVA $p < 0.001$) (Figure 3 K). This effect was strongest early in learning, as MEC odor-selectivity increased with DNMS performance (Pearson's $r = 0.373$). The larger number of odor selective axons in LEC resulted in better odor decoding during odor presentation when repetitively subsampling only 100 axons from each recording session (for all recordings LEC decoding accuracy was 57.0 $\pm$ 4.2% and MEC accuracy was 53.5 $\pm$ 2.2%, ANOVA $p < 0.001$; for only expert sessions LEC accuracy was 57.0 $\pm$ 4.3% and MEC accuracy was 54.4 $\pm$ 2.1%, ANOVA $p = 0.032$) (Figure 3 L-M). Again, decoding accuracy for LEC was stable across days and performance levels (Pearson's $r = 0.093$), but dramatically improved for MEC (Pearson's $r = 0.539$) (Figure 3 N). While odor decoding was worse during the delay period than during the odor presentation, decoding accuracy during the delay period remained significantly greater for LEC compared to MEC (for all recordings LEC accuracy was 54.8 $\pm$ 3.8% and MEC accuracy was 51.7 $\pm$ 1.5%, ANOVA $p < 0.001$; for only expert sessions LEC accuracy was 54.5 $\pm$ 4.1% and MEC accuracy was 52.0 $\pm$ 1.7%, ANOVA $p = 0.030$) (Figure 3 L-M and Figure S7 H). Increasing the number of subsampled axons for decoding led to improvements in odor decoding, but in general differences between LEC and MEC were similar across a large range of axon numbers subsampled for decoding analysis (Figure S7 I-J).

To understand if LEC and MEC encode other task relevant representations in our working memory task, we asked whether EC axons can encode whether the two odors matched or did not match. Both MEC and LEC axons showed an increase in SVM decoding accuracy of match versus non-match trials with increasing performance (LEC Pearson's $r = 0.382$ and MEC Pearson's $r = 0.746$); however, MEC accuracy was dramatically higher even during the 2nd odor which is one second before the start of the reward period (67.0 $\pm$ 7.4% for MEC, and 57.6 $\pm$ 6.2% for LEC, ANOVA $p < 0.001$). During poor performance sessions (<85% performance), match versus non-match trial decoding accuracy peaked during the middle of the reward period as the outcome was encoded, and MEC decoding accuracy was significantly higher than LEC (Figure S8 D). Interestingly, once mice reached expert performance, decoding accuracy of match versus non-match trials peaked during the 2nd odor for MEC, but still peaked during the reward period for LEC (Figure S8 E).

Altogether, these findings suggest that LEC temporammonic axonal odor representations were strong in novice animals and did not improve with performance, while MEC axonal firing became strongly tuned to firing at odor presentations during learning but had relatively weaker odor-selectivity. Meanwhile MEC but not LEC axons showed emergence of robust working memory representations related to reward, choice, or trial types.

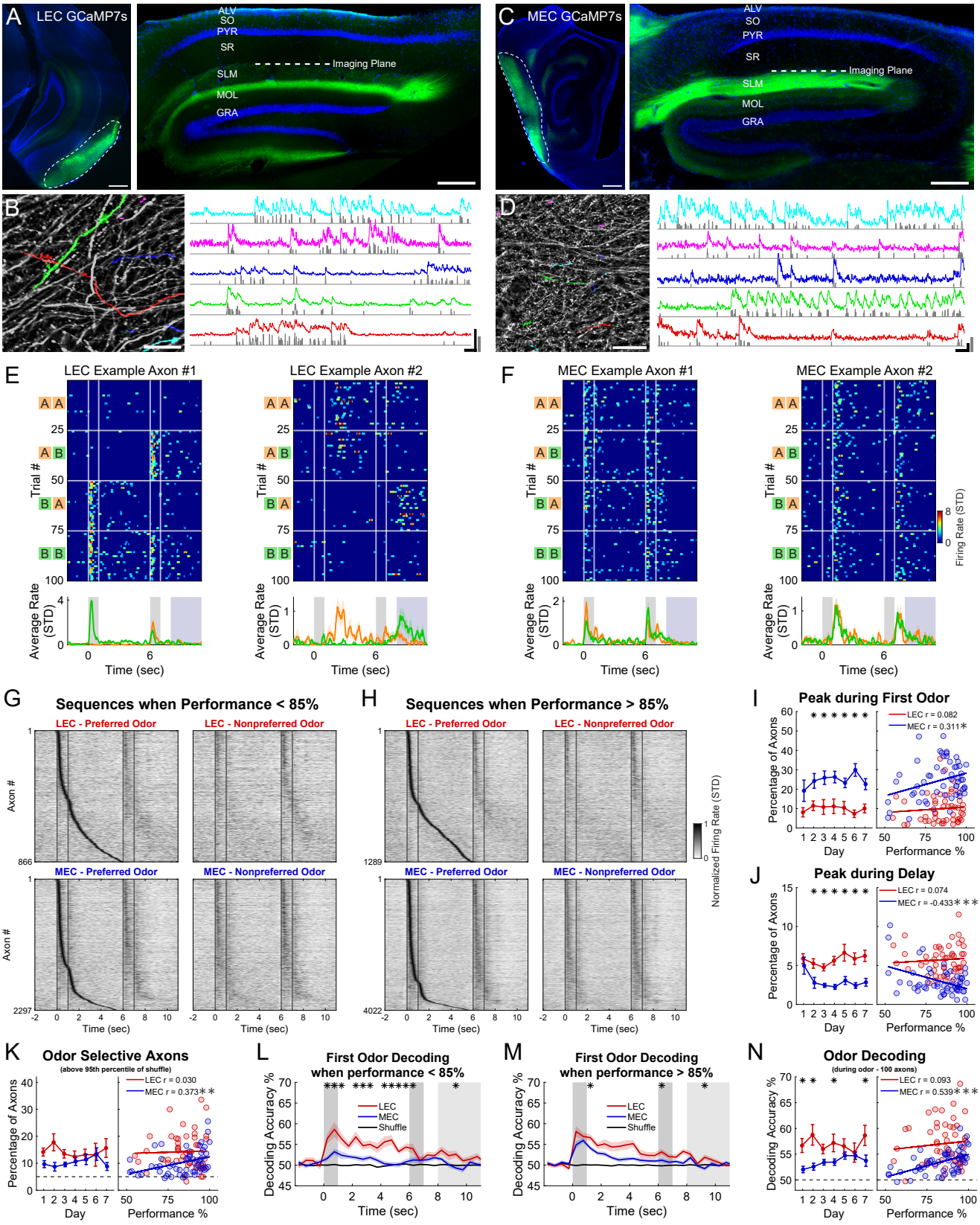
A
LEC GCaMP7s
ALV
SO
PYR
SR
SLM
MOL
GRA
Imaging Plane
C
MEC GCaMP7s
B
D
E
LEC Example Axon #1
LEC Example Axon #2
F
MEC Example Axon #1
MEC Example Axon #2
Trial #
Average Rate (STD)
Time (sec)
Firing Rate (STD)
G
Sequences when Performance < 85%
LEC - Preferred Odor
LEC - Nonpreferred Odor
MEC - Preferred Odor
MEC - Nonpreferred Odor
Axon #
H
Sequences when Performance > 85%
Normalized Firing Rate (STD)
I
Peak during First Odor
LEC r = 0.082
MEC r = 0.311
Percentage of Axons
Day
Performance %
J
Peak during Delay
LEC r = 0.074
MEC r = -0.433
K
Odor Selective Axons
(above 95th percentile of shuffle)
LEC r = 0.030
MEC r = 0.373
L
First Odor Decoding when performance < 85%
M
First Odor Decoding when performance > 85%
LEC
MEC
Shuffle
Decoding Accuracy %
N
Odor Decoding
(during odor - 100 axons)
LEC r = 0.093
MEC r = 0.539

Figure 3: Two-photon calcium imaging of entorhinal cortical axons in dorsal CA1 revealed differential sequential activity in LEC and MEC inputs. **A)** Coronal sections showing GCaMP7s expression LEC (left panel, scale bar = 500µm) and in dorsal hippocampus (right panel, scale bar = 250µm). Blue is DAPI. Imaging plane is at the superficial part of the SLM layer, which is the first layer of axons visible when lowering into the tissue roughly 300-400µm beneath the coverglass. ALV = alveus, SO = stratum oriens, PYR = stratum pyramidale, SR = stratum radiatum, SLM = stratum lacunosum-moleculare, MOL = stratum moleculare, GRA = stratum granulare. **B)** Field of view from the same animal (scale bar = 50µm), with 5 example masks and their corresponding fluorescence traces. Gray is z-scored deconvolved signal. Black horizontal scale bar = 10 seconds. Black vertical scale bar = 5% $\Delta F/F$. Gray vertical scale bar = 10 STD normalized deconvolved signal. **C-D)** Same as (A-B) but for MEC and showing sagittal sections. All scale bars are the same. **E)** Two example axon segments showing odor-specific firing. The left axon had its peak during the odor presentation, while the right one had its peak during the delay period. Heatmaps show deconvolved signal on each trial that was grouped into trial type. Average traces at bottom show difference in average firing rate split by trials that started with Odor A and those that started with Odor B. **F)** Same as (E) but for two representative MEC axon segments with less odor-selectivity. The right axon had its peak following the offset of the odor presentation. **G)** Sequential activity of only axon segments that had a significant peak during the first odor presentation or delay period from recording sessions with performance less than 85%. Each row is the average trace of trials with the preferred or nonpreferred first odor (normalized to peak). Blue lines indicate odor onset and offset. **H)** Same as (G) but when performance was at least 85%. **I)** Top panel is percentage of axons with a significant peak during the first odor presentation period. Bottom panel is percentage of axons with a significant peak during the delay period. Statistics for left panels are two-sample t-tests and p-values were corrected for multiple comparisons using the Benjamini-Hochberg procedure. Statistics for right panels are Pearsons' R correlation with performance. **K)** Percentage of axons that had a selectivity value above 95th percentile of shuffle. **L)** Binary SVM decoding of first odor across the trial structure with 0.5 second bins (repetitive subsampling 100 axons for each recording session), only on recordings sessions with behavior performance less than 85%. Statistics are two-way ANOVA (animal and day), and asterisks indicate bins with $p < 0.05$ (corrected for multiple comparisons using the Benjamini-Hochberg procedure). **M)** Same as (L) but when performance was at least 85%. **N)** Binary SVM odor decoding only during the odor presentation period (repetitive subsampling 100 axons for each recording session).

LEC and MEC inhibition slow representational drift of odor representations in dorsal CA1

Despite the similarity of LEC TA axon population dynamics across days, our previous work revealed that CA1 odor representations drift over days [18] with new neurons forming sensory relevant fields and other neurons losing their responsiveness or selectivity. Given that non-spatial BTSP can result in rapid generation of odor-selective responses, we hypothesized that it could play a role in representational drift. Since MEC inhibition reduces the frequency of 'plateau-like' events and LEC inhibition reduces the success rate of odor-field formation, we hypothesized that the reduction of BTSP events through EC inhibition may result in increased stability of representations. To address this hypothesis and compare representations over days, we matched dorsal CA1 neurons across 8 days of alternating saline and uPSEM administrations (Figure 4 A). While some BTSP events formed odor-fields that fade within the recording session (Figure 1 H and Figures S1-S2), others formed fields that lasted for several days (Figure 4 A-B). We used binary SVM decoders trained on the activity of 100 randomly chosen neurons on the day before EC inhibition (Saline Day X) and tested on the same neurons the day after EC inhibition (48 hours later on Saline Day X+2). We compared these results to same-day decoding on Saline Day X. The higher the success rate of the decoder for across-day decoding, the more stable the representation.

In control mice expressing mCherry, decoder accuracy declined quickly (77.0 $\pm$ 6.4% for same-day decoding (Saline Day X) to 58.2 $\pm$ 9.7% for across-day decoding two days later (Saline Day X+2) (Figure 4 B-C)), suggesting substantial representational drift. In experimental mice expressing PSAM4, decoder accuracy dropped substantially less for LEC (76.4 $\pm$ 11.0% for same-day decoding to 65.1 $\pm$ 10.1% for across-day decoding two days later) and MEC (79.0 $\pm$ 5.8% for same-day decoding to 65.0 $\pm$ 4.6% for across-day decoding two days later). In addition, the percentage of Saline Day X neurons that remain significantly odor selective on Saline Day X+2 was higher in LEC experimental PSAM4 animals (45.4 $\pm$ 10.9%) than in control mCherry animals (36.3 $\pm$ 9.9%) (Figure 4 E). This indicates that PSAM4 inhibition of both LEC or MEC decreased representational drift across a 48-hour period.

In summary, MEC inhibition reduced large calcium events in CA1, LEC inhibition decreased success rate of these 'plateau-like' events, and inhibition of either LEC or MEC slowed representational drift of odor in CA1. These findings suggest that drift of CA1 olfactory representations is modulated by EC inputs, potentially from decreased non-spatial BTSP.

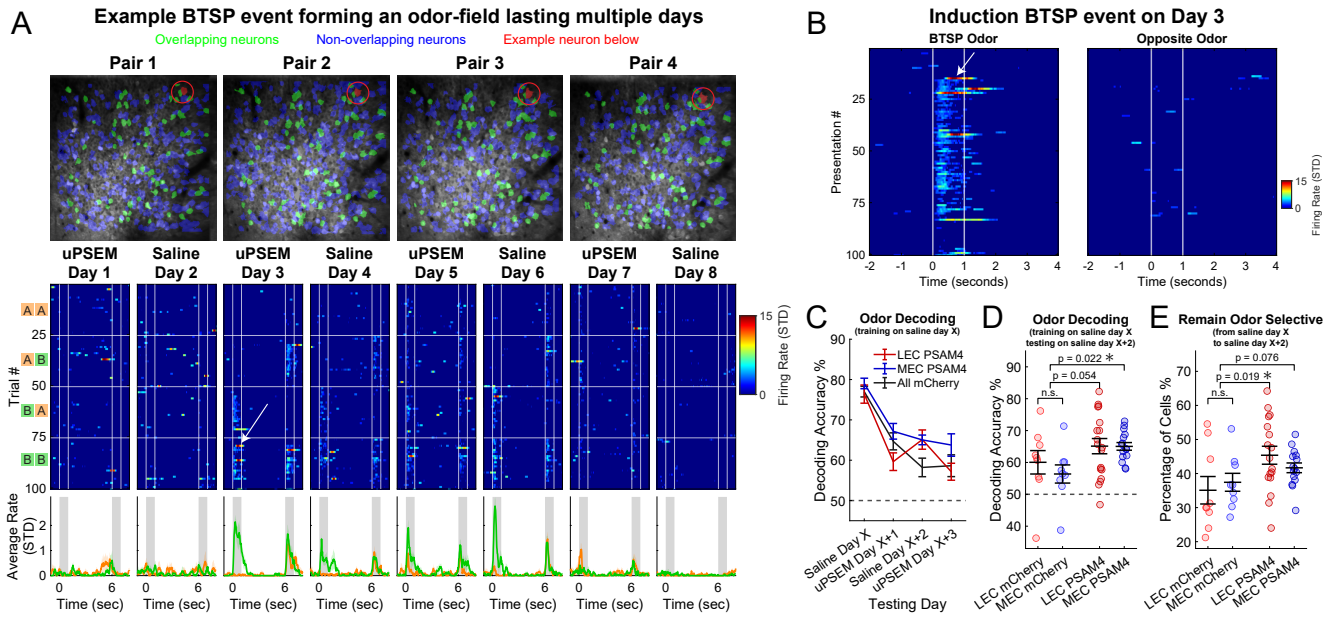

Figure 4: LEC and MEC inhibition both slow representational drift of odor representations in dorsal CA1. **A)** Example CA1 neuron across 8 days of expert performance. The 4 FOV images show the masks used for each 'pair' (see methods), and neurons were aligned across pairs with CellReg [42]. Green masks are neurons that overlap in all 4 pairs; blue masks do not overlap in all 4 pairs, and the single red mask is the example neuron with activity below. Heatmaps show deconvolved signal on each trial with trials grouped according to DNMS odor combinations. Average traces at bottom show average firing rates for trials that started with Odor A (orange) or with Odor B (green). **B)** Visualization of BTSP event in Day 3 from (A) that is likely reinforced by several strong 'plateau-like' events. The white arrow points to the same induction 'plateau-like' event as the white arrow in (A). **C)** Binary SVM decoding of odor (only during odor presentation periods) after training on saline day X (repetitive random subsampling of 100 neurons for each recording session). **D)** Highlighting the effect in (C) on saline day X+2 with each circle representing a recording session. Black bars represent mean and standard error of the mean (SEM). Statistics are two-way ANOVA (animal and pair). **E)** Percentage of neurons that have odor-selectivity values that remained above 90th percentile of shuffle for their preferred odor.

DISCUSSION

Using two-photon calcium imaging of dorsal CA1 pyramidal neurons during an olfactory working memory task, we find that non-spatial sensory representations can form on single trials following large calcium events. These events have characteristics of BTSP reported previously during spatial tasks [3, 4, 5, 6, 7, 8, 9, 10], suggesting that BTSP may be a general plasticity mechanism for formation of hippocampal representations during both spatial and non-spatial cognition. Additionally, MEC and LEC inhibition differentially modulate non-spatial BTSP during working memory performance. MEC inhibition decreases the frequency of large 'plateau-like' calcium events, while LEC inhibition reduces the success rate of these 'plateau-like' events generating an odor-field. LEC inputs are critical for generation of odor representations in CA1, with LEC inhibition dramatically weakening CA1 odor-selectivity and odor encoding. This may contribute to their modulation of BTSP success rate in generating odor-selective responses. By performing two-photon calcium imaging of LEC or MEC temporammonic pathway axons to CA1, we show that LEC relays stronger odor-specific information to CA1 that is invariant in learning and expert stages, while MEC axonal activity shows greater plasticity with learning, increasing odor and match/non-match selectivity and tuning to more reliably fire during the odor presentations. Finally, inhibition of either LEC or MEC leads to reduced representational drift of CA1 odor representations, suggesting that BTSP (or another EC-dependent plasticity process) can modulate representational drift.

This is to our knowledge the first description of behavioral timescale synaptic plasticity (BTSP) occurring in a non-spatial context. Non-spatial BTSP described in this paper and spatial BTSP described in spatial contexts [3, 4, 5, 6, 7, 8, 9, 10] share many attributes. First, they are both induced by large calcium events. Second, like spatial BTSP, odor-responsive fields typically form around 0.5 seconds before the time of onset of the 'plateau-like' event. This temporally asymmetric induction of fields is characteristic of BTSP in CA1. Membrane potential (Vm) recordings in CA1 during spatial BTSP demonstrate potentiation causing the induction of an asymmetric Vm ramp extending back nearly 4 seconds from the timepoint of induction. Voltage recordings would be required to determine whether a Vm ramp extending several seconds is also induced by non-spatial BTSP. There are notable differences between spatial and non-spatial BTSP, however. While spatial BTSP can induce place fields anywhere in the virtual track, during our non-spatial BTSP, 86% of successful fields were formed during or immediately after the odor presentations, with few fields formed during the delay and reward periods. It is possible that this occurs because subthreshold inputs potentiated by BTSP in the delay period fail to reach action potential threshold. This could be explained by the fewer EC inputs activated during the delay period as LEC has nearly twice as many axons and MEC nearly 10 times as many axons with peak firing during the odor period compared to the delay period. Recordings of Vm during the task would be necessary to find whether the magnitude of synaptic potentiation is similar during the different phases of the task. It also remains to be determined whether TA inputs, CA3 inputs, or both are potentiated during non-spatial BTSP. Finally, while inhibitory interneuron subtypes have been characterized by their roles in gating spatial EC and CA3 inputs to CA1 [43, 44, 45, 46], it remains unclear how the different interneuron subtypes within the different layers of CA1 contribute to BTSP and gate non-spatial sensory inputs. Future recordings and manipulations of the activity of these neurons will further elucidate the complex mechanisms underlying non-spatial BTSP in CA1.

We find that inhibition of LEC and MEC have distinct effects on non-spatial BTSP. While MEC inhibition reduces the frequency of large calcium events, LEC inhibition has no impact on the frequency or amplitude of these events but reduces their success rate in generating odor-fields. Therefore, while it is clear that MEC plays a major role in generating the plateau potential teaching signal with most of its activity timed to stimulus presentations, the exact mechanism through which LEC regulates the success of BTSP events is less clear. There are several possibilities. It is possible that BTSP

potentiates the LEC inputs on the distal dendrites of CA1 pyramidal neuron which aids in generating odor-selective responses. Alternatively, it is possible that LEC inhibition reduces odor-selectivity and the amplitude of odor responses in dentate gyrus granule neurons or in CA3, which in turn reduces the potentiation of CA3 inputs to CA1. Our results are in line with studies which have shown the importance of MEC inputs for generation of teaching signals to drive BTSP during spatial learning tasks [7, 9], but our results describe the further complexity given the distinct roles of LEC and MEC.

We found that CA1 population odor representations were more stable the day after MEC or LEC inhibition, suggesting that EC inhibition slows representational drift. This reduction can potentially occur through a reduction in frequency or success rate of BTSP events, as shown in our work, or may occur through a different plasticity mechanism governed by EC activation [47, 48, 49]. While BTSP can clearly explain the appearance of a new field, the mechanism for erasure of existing fields remains less clear. One possibility is that decreases in synaptic weights can occur following mistimed plateau potentials, given that spatial BTSP has been shown to increase synaptic weights of inputs within 2 seconds of a plateau and decrease synaptic weights of inputs between 2 and 5 seconds of the plateau [8]. However, a continuing challenge for the field will be to understand the complex interplay of other plasticity mechanisms implicated in representational drift that operate on different and longer timescales, such as Hebbian spike timing-dependent plasticity that includes long-term potentiation (LTP) and long-term depression (LTD) [50, 51, 52] or dendritic spine turnover [53, 54, 55]. There is some evidence that there are distinct pools of CA1 neurons with short or long place field lifetimes, which may be related to BTSP success rate [56]. Whether similar pools exist for non-spatial representation remains to be determined.

Our findings support the structural and functional connectivity of LEC and the hippocampus in olfactory based tasks [30, 31, 32, 33], but further experiments with other modalities would be valuable in establishing LEC and MEC's unique roles in driving plateau potentials and forming non-spatial representational fields. CA1 is also well known for its internal representations [19, 20, 21]. Although we observed some BTSP events that form odor-specific fields during the delay period, future recordings should investigate if LEC and MEC inputs coincide with the output from recurrent CA3 networks capable of generated temporal codes [57, 58, 59] to drive BTSP for internally generated representations.

ACKNOWLEDGMENTS

We thank D. Buonomano, G. Orban, and S. Miller-Hecht for feedback on the manuscript. We also thank B. Madruga, Z. Day, X. Chen, and C. Yang for technical support. This work was supported by the following funding sources: T32DGE1829071, 5T32NS045540-20, R01NS116589, and 1P50HD103557-01.

AUTHOR CONTRIBUTIONS

C.D., J.T., and P.G. conceived the experiments. C.D. conducted experiments, analyzed experimental data, and generated the figures. C.D. and P.G. wrote the manuscript.

DECLARATION OF INTERESTS

The authors declare no competing interests.

References

[1] B. M. Lake, R. Salakhutdinov, J. B. Tenenbaum, Human-level concept learning through probabilistic program induction, Science 350 (6266) (2015) 1332–1338.

[2] Y. Song, T. Wang, P. Cai, S. K. Mondal, J. P. Sahoo, A comprehensive survey of few-shot learning: Evolution, applications, challenges, and opportunities, ACM Computing Surveys 55 (13s) (2023) 1–40.

[3] K. C. Bittner, C. Grienberger, S. P. Vaidya, A. D. Milstein, J. J. Macklin, J. Suh, S. Tonegawa, J. C. Magee, Conjunctive input processing drives feature selectivity in hippocampal ca1 neurons, Nature neuroscience 18 (8) (2015) 1133–1142.

[4] K. C. Bittner, A. D. Milstein, C. Grienberger, S. Romani, J. C. Magee, Behavioral time scale synaptic plasticity underlies ca1 place fields, Science 357 (6355) (2017) 1033–1036.

[5] C. Grienberger, A. D. Milstein, K. C. Bittner, S. Romani, J. C. Magee, Inhibitory suppression of heterogeneously tuned excitation enhances spatial coding in ca1 place cells, Nature neuroscience 20 (3) (2017) 417–426.

[6] X. Zhao, Y. Wang, N. Spruston, J. C. Magee, Membrane potential dynamics underlying context-dependent sensory responses in the hippocampus, Nature neuroscience 23 (7) (2020) 881–891.

[7] J. C. Magee, C. Grienberger, Synaptic plasticity forms and functions, Annual review of neuroscience 43 (2020) 95–117.

[8] A. D. Milstein, Y. Li, K. C. Bittner, C. Grienberger, I. Soltesz, J. C. Magee, S. Romani, Bidirectional synaptic plasticity rapidly modifies hippocampal representations, Elife 10 (2021) e73046.

[9] C. Grienberger, J. C. Magee, Entorhinal cortex directs learning-related changes in ca1 representations, Nature 611 (7936) (2022) 554–562.

[10] K. Xiao, Y. Li, R. A. Chitwood, J. C. Magee, A critical role for camkii in behavioral timescale synaptic plasticity in hippocampal ca1 pyramidal neurons, Science Advances 9 (36) (2023) eadi3088.

[11] J. O'Keefe, J. Dostrovsky, The hippocampus as a spatial map: preliminary evidence from unit activity in the freely-moving rat., Brain research (1971).

[12] E. R. Wood, P. A. Dudchenko, H. Eichenbaum, The global record of memory in hippocampal neuronal activity, Nature 397 (6720) (1999) 613–616.

[13] G. Buzsáki, D. Tingley, Space and time: the hippocampus as a sequence generator, Trends in cognitive sciences 22 (10) (2018) 853–869.

[14] E. I. Moser, M.-B. Moser, B. L. McNaughton, Spatial representation in the hippocampal formation: a history, Nature neuroscience 20 (11) (2017) 1448–1464.

[15] R. E. Hampson, J. D. Simeral, S. A. Deadwyler, Distribution of spatial and nonspatial information in dorsal hippocampus, Nature 402 (6762) (1999) 610–614.

[16] L. R. Squire, Memory and the hippocampus: a synthesis from findings with rats, monkeys, and humans., Psychological review 99 (2) (1992) 195.

[17] D. Aronov, R. Nevers, D. W. Tank, Mapping of a non-spatial dimension by the hippocampal–entorhinal circuit, Nature 543 (7647) (2017) 719–722.

[18] J. Taxidis, E. A. Pnevmatikakis, C. C. Dorian, A. L. Mylavarapu, J. S. Arora, K. D. Samadian, E. A. Hoffberg, P. Golshani, Differential emergence and stability of sensory and temporal representations in context-specific hippocampal sequences, Neuron 108 (5) (2020) 984–998.

[19] E. Pastalkova, V. Itskov, A. Amarasingham, G. Buzsaki, Internally generated cell assembly sequences in the rat hippocampus, Science 321 (5894) (2008) 1322–1327.

[20] C. J. MacDonald, K. Q. Lepage, U. T. Eden, H. Eichenbaum, Hippocampal “time cells” bridge the gap in memory for discontiguous events, Neuron 71 (4) (2011) 737–749.

[21] H. Eichenbaum, Time cells in the hippocampus: a new dimension for mapping memories, Nature Reviews Neuroscience 15 (11) (2014) 732–744.

[22] T. V. Bliss, T. Lømo, Long-lasting potentiation of synaptic transmission in the dentate area of the anaesthetized rabbit following stimulation of the perforant path, The Journal of physiology 232 (2) (1973) 331–356.

[23] N. Caporale, Y. Dan, Spike timing–dependent plasticity: a hebbian learning rule, Annu. Rev. Neurosci. 31 (1) (2008) 25–46.

[24] M. Mayford, S. A. Siegelbaum, E. R. Kandel, Synapses and memory storage, Cold Spring Harbor perspectives in biology 4 (6) (2012) a005751.

[25] D. E. Feldman, The spike-timing dependence of plasticity, Neuron 75 (4) (2012) 556–571.

[26] S. S. Deshmukh, J. J. Knierim, Representation of non-spatial and spatial information in the lateral entorhinal cortex, Frontiers in behavioral neuroscience 5 (2011) 69.

[27] J. J. Knierim, J. P. Neunuebel, S. S. Deshmukh, Functional correlates of the lateral and medial entorhinal cortex: objects, path integration and local–global reference frames, Philosophical Transactions of the Royal Society B: Biological Sciences 369 (1635) (2014) 20130369.

[28] P. Andersen, R. Morris, D. Amaral, T. Bliss, J. O’Keefe, The hippocampus book, Oxford university press, 2007.

[29] N. Van Strien, N. Cappaert, M. Witter, The anatomy of memory: an interactive overview of the parahippocampal–hippocampal network, Nature reviews neuroscience 10 (4) (2009) 272–282.

[30] K. M. Igarashi, L. Lu, L. L. Colgin, M.-B. Moser, E. I. Moser, Coordination of entorhinal–hippocampal ensemble activity during associative learning, Nature 510 (7503) (2014) 143–147.

[31] Y. Li, J. Xu, Y. Liu, J. Zhu, N. Liu, W. Zeng, N. Huang, M. J. Rasch, H. Jiang, X. Gu, et al., A distinct entorhinal cortex to hippocampal ca1 direct circuit for olfactory associative learning, Nature neuroscience 20 (4) (2017) 559–570.

[32] N. I. Woods, F. Stefanini, D. L. Apodaca-Montano, I. M. Tan, J. S. Biane, M. A. Kheirbek, The dentate gyrus classifies cortical representations of learned stimuli, Neuron 107 (1) (2020) 173–184.

[33] Y. J. Zhang, J. Y. Lee, K. M. Igarashi, Circuit dynamics of the olfactory pathway during olfactory learning, Frontiers in Neural Circuits 18 (2024) 1437575.

[34] M. Fyhn, S. Molden, M. P. Witter, E. I. Moser, M.-B. Moser, Spatial representation in the entorhinal cortex, Science 305 (5688) (2004) 1258–1264.

[35] T. Hafting, M. Fyhn, S. Molden, M.-B. Moser, E. I. Moser, Microstructure of a spatial map in the entorhinal cortex, Nature 436 (7052) (2005) 801–806.

[36] F. Sargolini, M. Fyhn, T. Hafting, B. L. McNaughton, M. P. Witter, M.-B. Moser, E. I. Moser, Conjunctive representation of position, direction, and velocity in entorhinal cortex, Science 312 (5774) (2006) 758–762.

[37] T. Cholvin, T. Hainmueller, M. Bartos, The hippocampus converts dynamic entorhinal inputs into stable spatial maps, Neuron 109 (19) (2021) 3135–3148.

[38] D. Liu, X. Gu, J. Zhu, X. Zhang, Z. Han, W. Yan, Q. Cheng, J. Hao, H. Fan, R. Hou, et al., Medial prefrontal activity during delay period contributes to learning of a working memory task, Science 346 (6208) (2014) 458–463.

[39] M. Pachitariu, C. Stringer, M. Dipoppa, S. Schröder, L. F. Rossi, H. Dalgleish, M. Carandini, K. D. Harris, Suite2p: beyond 10,000 neurons with standard two-photon microscopy, bioRxiv (2017). arXiv:https://www.biorxiv.org/content/early/2017/07/20/061507.full.pdf, doi:10.1101/061507.

[40] H. Takahashi, J. C. Magee, Pathway interactions and synaptic plasticity in the dendritic tuft regions of ca1 pyramidal neurons, Neuron 62 (1) (2009) 102–111.

[41] C. J. Magnus, P. H. Lee, J. Bonaventura, R. Zemla, J. L. Gomez, M. H. Ramirez, X. Hu, A. Galvan, J. Basu, M. Michaelides, et al., Ultrapotent chemogenetics for research and potential clinical applications, Science 364 (6436) (2019) eaav5282.

[42] L. Sheintuch, A. Rubin, N. Brande-Eilat, N. Geva, N. Sadeh, O. Pinchasof, Y. Ziv, Tracking the same neurons across multiple days in ca2+ imaging data, Cell reports 21 (4) (2017) 1102–1115.

[43] T. Klausberger, P. Somogyi, Neuronal diversity and temporal dynamics: the unity of hippocampal circuit operations, Science 321 (5885) (2008) 53–57.

[44] A. Kepecs, G. Fishell, Interneuron cell types are fit to function, Nature 505 (7483) (2014) 318–326.

[45] A. D. Milstein, E. B. Bloss, P. F. Apostolides, S. P. Vaidya, G. A. Dilly, B. V. Zemelman, J. C. Magee, Inhibitory gating of input comparison in the ca1 microcircuit, Neuron 87 (6) (2015) 1274–1289.

[46] J. Basu, J. D. Zaremba, S. K. Cheung, F. L. Hitti, B. V. Zemelman, A. Losonczy, S. A. Siegelbaum, Gating of hippocampal activity, plasticity, and memory by entorhinal cortex long-range inhibition, Science 351 (6269) (2016) aaa5694.

[47] M. E. Rule, T. O'Leary, C. D. Harvey, Causes and consequences of representational drift, Current opinion in neurobiology 58 (2019) 141–147.

[48] L. N. Driscoll, L. Duncker, C. D. Harvey, Representational drift: Emerging theories for continual learning and experimental future directions, Current Opinion in Neurobiology 76 (2022) 102609.

[49] C. Micou, T. O'Leary, Representational drift as a window into neural and behavioural plasticity, Current opinion in neurobiology 81 (2023) 102746.

[50] D. Kappel, S. Habenschuss, R. Legenstein, W. Maass, Network plasticity as bayesian inference, PLoS computational biology 11 (11) (2015) e1004485.

[51] L. Aitchison, J. Jegminat, J. A. Menendez, J.-P. Pfister, A. Pouget, P. E. Latham, Synaptic plasticity as bayesian inference, Nature neuroscience 24 (4) (2021) 565–571.

[52] S. Qin, S. Farashahi, D. Lipshutz, A. M. Sengupta, D. B. Chklovskii, C. Pehlevan, Coordinated drift of receptive fields in hebbian/anti-hebbian network models during noisy representation learning, Nature Neuroscience 26 (2) (2023) 339–349.

[53] N. Yasumatsu, M. Matsuzaki, T. Miyazaki, J. Noguchi, H. Kasai, Principles of long-term dynamics of dendritic spines, Journal of Neuroscience 28 (50) (2008) 13592–13608.

[54] A. Minerbi, R. Kahana, L. Goldfeld, M. Kaufman, S. Marom, N. E. Ziv, Long-term relationships between synaptic tenacity, synaptic remodeling, and network activity, PLoS biology 7 (6) (2009) e1000136.

[55] A. Attardo, J. E. Fitzgerald, M. J. Schnitzer, Impermanence of dendritic spines in live adult ca1 hippocampus, Nature 523 (7562) (2015) 592–596.

[56] S. P. Vaidya, R. A. Chitwood, J. C. Magee, The formation of an expanding memory representation in the hippocampus, bioRxiv (2023). arXiv:https://www.biorxiv.org/content/early/2023/02/02/2023.02.01.526663.full.pdf, doi:10.1101/2023.02.01.526663.

[57] J. K. Liu, D. V. Buonomano, Embedding multiple trajectories in simulated recurrent neural networks in a self-organizing manner, Journal of Neuroscience 29 (42) (2009) 13172–13181.

[58] A. Holtmaat, P. Caroni, Functional and structural underpinnings of neuronal assembly formation in learning, Nature neuroscience 19 (12) (2016) 1553–1562.

[59] D. M. Salz, Z. Tiganj, S. Khasnabish, A. Kohley, D. Sheehan, M. W. Howard, H. Eichenbaum, Time cells in hippocampal area ca3, Journal of Neuroscience 36 (28) (2016) 7476–7484.

RESOURCE AVAILABILITY

Lead Contact

Further information and requests for resources and reagents should be directed to the Lead Contact, Peyman Golshani (pgolshani@mednet.ucla.edu).

Material Availability

No new materials were created for this study.

Data and Code Availability

The data and analysis code generated in this study are available upon request to the corresponding authors.

EXPERIMENTAL MODEL AND SUBJECT DETAILS

Animals

All of the experiments were conducted according to the National Institute of Health (NIH) guidelines and with the approval of the Chancellor's Animal Research Committee of the University of California, Los Angeles. A total of 9 adult male and 8 female mice (8-16 weeks old) were used for *in-vivo* calcium CA1 neuron imaging experiments, and a total of 7 adult male and 9 female mice (8-16 weeks old) were used for *in-vivo* calcium EC axon imaging experiments. CA1 imaging mice are divided into 4 groups: LEC mCherry n=3, MEC mCherry n=3, LEC PSAM4 n=6, MEC PSAM4 n=5. Axon imaging mice are divided into 2 groups: LEC n=8, MEC n=8. All were C57BL/6J (Jackson Laboratory, 000664), experimentally naïve, and housed in the vivarium under a 12-hour light/dark cycle. All mice were group housed (2-4 per cage) with the exception of 2 that had to be separated following surgery because of fighting.

METHOD DETAILS

Surgical Procedures

Mice (8-12 weeks old) were subcutaneously administered pre-operative drugs (carprofen 5 mg/kg, dexamethasone 0.2 mg/kg, lidocaine 5 mg/kg) 30 minutes before surgery. Mice were anaesthetized with isoflurane (5% induction, 1-2% for maintenance), and anesthesia was continuously monitored and adjusted as necessary. The scalp was shaved, and mice were placed into a stereotactic frame (David Kopf Instruments, Tujunga, CA) on a feedback-controlled heating pad (Harvard Apparatus) set to maintain body temperature at 37°C. Eyes were protected from desiccation using artificial tear ointment. The surgical incision site was cleaned three times with 10% povidone-iodine and 70% ethanol. Fascia was removed by applying hydrogen peroxide, connective tissue was cleared from the skull, and the skull was scored to facilitate effective bonding with adhesives at the end of surgery. After stereotactically aligning the skull, a single or several burr holes were made depending on the experiment performed and virus was injected.

CA1 calcium imaging experiments: Control virus (500 nL of 1:5 saline dilution of pAAV1-CaMKIIa-mCherry into all 4 sites) or experimental virus (500 nL of 1:5 saline dilution of AAV5-CaMKII-PSAM4-GlyR-IRES-EGFP into all 4 sites) was injected into LEC (bilaterally 3.4 and 3.9 mm posterior, 4.35 mm lateral, and 4.3 ventral from bregma) or MEC (bilaterally 4.7 mm posterior, 3.35 mm lateral, and 3.8 and 3.0 mm ventral from bregma). Additionally, pGP-AAV1-syn-jGCaMP8f-WPRE

(1000nL of 1:5 saline dilution) was injected into the right dorsal CA1 (2.0 mm posterior from bregma, 1.8 lateral from bregma, and 1.3 ventral from dura).

EC axon calcium imaging experiments: pENN.AAV1.CaMKII.0.4.Cre.SV40 and pGP-AAV1-CAG-FLEX-jGCaMP7f-WPRE were mixed immediately before the injection (500 nL of 1:1 mix) into right LEC (3.5 mm posterior, 4.35 mm lateral, and 4.3 ventral from bregma) or right MEC (4.7 mm posterior, 3.35 mm lateral, and 3.5 mm ventral from bregma). All viruses were injected using a Nanoject II microinjector (Drummond Scientific) at 60nL per minute.

For mice in all experiments, following virus injection, a circular craniotomy (3 mm diameter) was made centered around a point made 2.0 mm posterior and 1.8 lateral to bregma. Dura beneath the craniotomy was removed and cortical tissue above dorsal CA1 was carefully aspirated using a 27-gauge blunt needle. Corpus callosum was spread to the sides of the craniotomy to expose the alveus. Cortex buffer (NaCl = 7.88g/L, KCl = 0.372g/L, HEPES = 1.192g/L, $CaCl_2$ = 0.264g/L, $MgCl_2$ = 0.204g/L, at a pH of 7.4) was continuously flushed during aspiration and until bleeding stopped. A titanium ring with a 3 mm diameter circular thin #0 coverglass attached to its bottom was implanted into the aspirated craniotomy and the overhanging flange was secured to the skull with vetbond (3M). A custom-made lightweight stainless-steel headbar was attached to posterior skull and secured with cyanoacrylate glue. Dental cement (Ortho-Jet, Lang Dental) was applied to seal and cover any remaining skull, and to form a small well around the titanium ring for holding immersion water for the objective during imaging. Following surgery, all animals were given post-operative care (carprofen 5 mg/kg and dexamethasone 0.2 mg/kg for 48 hours after surgery) and provided amoxicillin-treated water at 0.5 mg/mL for 7 days. All mice recovered for 7-14 days before experiments began.

Experimental setup

The entire behavioral setup is as described in Taxidis et al. [18]. Mice were head-fixed above an 8-inch spherical Styrofoam ball (Graham Sweet) which can rotate about one axis for 1D locomotion that was recorded with a sensor (Avago ADNS-9500). A continuous stream of clean air ($\sim$1 L/min) was delivered toward the animal's nose via Tygon PVC clear tubing and a custom-made port that held the air tube and water port. At the onset of the odor presentation period, a dual synchronous 3-way valve (NResearch) switched to the odorized one for 1 second. Odorized air was created by using a 4-ports olfactometer (Rev. 7c; Biology Electronics, Caltech) supplying air to either of two glass vials containing odor A (70% isoamyl acetete basis, FCC; Sigma Aldrich) or odor B ((-)-a-Pinene $\geq$ 97%, FCC; Sigma Aldrich), which were both diluted in mineral oil at 5% concentration. Water droplets ($\sim$10µl) were released by a 3-way solenoid valve (Lee Company), and licks were detected by using a custom battery-operated circuit board with one end of the circuit connected to the headbar and the other to the lickport. The behavioral rig was controlled with custom written software (MATLAB) and through a data acquisition board (USB-6341: National Instruments).

Behavioral training

After 7-14 days recovering from surgery, mice were handled and began water-restriction to 85% of their original weight before water-restriction. After one day of handling, mice were habituated to being head-fixed above the spherical treadmill for two days. On the 4th day of training, mice began learning to lick from the lickport as water was automatically delivered at the beginning of the reward period following only non-matched odor trials (AB or BA, with water delivery at time point of 8 seconds). Trials were delivered in blocks of 20 trials. This phase was always 2 days except for the rare mouse that needed one extra day to reach motivation level and lick water from the port for at least 50 trials. In the next phase, water was only delivered if the mouse licked during the response period, and mice learned

to reliably lick in anticipation of the reward following the 2nd odor. This phase was also 2 or 3 days, dependent on the mouse licking during the response period of at least 50 trials. The final phase was the full delayed non-match-to-sample (DNMS) task in which matched odor trials (AA and BB) were introduced and mice learned to refrain from licking the port following these trials. There was no punishment or timeout following an incorrect lick; the water was simply not delivered. The first day of this final full DNMS task was considered 'Day 1' in the axon imaging experiments (6-8 days from the start of water-deprivation). A total of 100 trials delivered in five blocks of 20 trials were given each day, and we considered 'expert performance' to be any day with performance greater than or equal to 85%. In the CA1 imaging experiments, two-photon calcium imaging only began after the mouse had 2 consecutive days of 'expert performance'. Mice underwent 5-7 days of learning the full DNMS task before recording began.

***In-vivo* two-photon imaging**

All two-photon calcium imaging was conducted using a resonant scanning two-photon microscope (Scientifica) fitted with a 16x 0.80 NA objective (Nikon) to record 512x512 pixel frames at 30.9 Hz. CA1 imaging fields of view were 500x500 µm and axonal imaging fields were 250x250 µm. Excitation light was delivered with a Ti:sapphire excitation laser (Chameleon Ultra II, Coherent), operated at 920 nm. GCaMP8f and GCaMP7s fluorescence was recorded with a green channel gallium arsenide photomultiplier tube (GaAsP PMT; Hamamatsu). Microscope control and image acquisition were performed using LabView-based software (SciScan). Imaging and behavioral data were synchronized by recording TTL pulses generated at the onset of each imaging frame and olfactory stimulation digital signals at 1 kHz, using WinEDR software (Strathclyde Electrophysiology Software).

For CA1 imaging experiments, a single field of view (FOV) was imaged for 8 consecutive days of expert performance. Careful attention was given to aligning the FOV to the previous day's as perfectly as possible. Animals were not included in analysis if successful alignment was not possible. We used rotating stages, a motor for adjusting mouse head angle, and a tiltable objective attachment with two degrees of freedom to fine-tune the alignment. For axonal imaging experiments, the same alignment was always attempted for 7 consecutive days of learning, but the extra difficulty of alignment made it not always possible. Therefore, axon segments were not registered between days; however, FOVs were typically very similar. Laser power and PMT settings were kept consistent between days, except for rare occasions when it was necessary to keep similar signal-to-noise. Out of the 16 axonal imaging animals included in analysis (each recorded for 7 days), 7 recording sessions were not included because of poor signal-to-noise.

For each day of recording, imaging was halted between each of the 5 blocks of 20 trials. This allowed fine-tuning of alignment, and it also prevented brain heating or photo-toxicity. Laser power was kept as minimal as possible (60-80mW for CA1, and 100-200mW for EC axons) without sacrificing signal-to-noise ratio, and only mild photo-bleaching was observed in some axonal imaging animals.

Chemogenetic inhibition

All CA1 imaging animals received subcutaneous injections of saline for at least 5 days prior to imaging to habituate them to the injection prior to being head-fixed. For the 8 days of imaging, mice received alternating injections of saline and uPSEM (ultrapotent PSEM 792 hydrochloride binds to PSAM4 to cause strong inhibition). Half of the mice started with saline and the other half started with uPSEM on the first day of imaging. The uPSEM powder was dissolved into saline at a concentration of 0.3 mg/mL, and injections were administered to achieve 3 mg/kg. After weighing the mouse to calculate the appropriate volume of saline or uPSEM, the mouse was injected intraperitoneally and head-fixed under the microscope. 10-20 minutes elapsed between the injection and the start of behavior.

Histology

Following all experiments, mice were deeply anaesthetized under isoflurane and transcardially perfused with 30 mL 1x PBS followed by 30 mL 4% paraformaldehyde in 1x PBS at a rate of approximately 4 mL/min. After perfusion, the brains were extracted and post-fixed in 4% paraformaldehyde. Sections of 80 µm were collected using a vibratome, 24-48 hours after perfusion. For animals with LEC viral expression, coronal sections were taken, while sagittal sections were taken from animals with MEC viral expression. The sections were mounted onto glass slides and cover-slipped with DAPI mounting medium. Images were acquired on an Apotome2 microscope (Zeiss; 5x, 10x, 20x objectives) to confirm proper expression and location of viral expression. For CA1 imaging experiments, GCaMP8f was confirmed to be in dorsal CA1, and sufficient PSAM4 or mCherry expression was found restricted to either LEC or MEC. In axonal imaging experiments, somatic GCaMP7s was confirmed to be restricted to only LEC or MEC, and axonal expression was found in the SLM layer of dorsal hippocampus. Mice with insufficient PSAM4/mCherry expression or PSAM4/mCherry/GCaMP7s that spread to outside of their desired target were excluded from analysis.

QUANTIFICATION AND STATISTICAL ANALYSIS

Calcium imaging data pre-processing

For CA1 imaging experiments, the 8 days of recordings were divided into 4 pairs of days, so that each pair consisted of one saline day and one uPSEM day. Both recordings from a single pair were concatenated before processing so that the same neurons could be detected within the pair of imaging days. Concatenated movies were processed using the Python implementation of Suite2P 0.9.2 [39] to perform non-rigid motion registration, neuron segmentation, extraction of fluorescence signals, and deconvolution with parameters optimized to our GCaMP8f CA1 recordings. We used the default classifier and an ‘iscell’ threshold of 0.1 to only include masks that were likely neurons. Neuron masks were then aligned across the 4 pairs of days using CellReg [42]. Because FOVs themselves were more helpful than the cell masks alone, we modified the CellReg code to do alignment based on the Suite2P registered mean image of the FOV. This yielded excellent registration for all animals with the maximal centroid distance set to 5 µm.

For axonal imaging experiments, the 7 days of recordings were all processed separately. Movies were also processed using Suite2P but with parameters optimized to our GCaMP7s axonal recordings. An additional step of axon merging was taken to decrease the number of duplicates (as an axon could appear as multiple segments within the FOV); this also increased signal-to-noise by increasing the number of pixels for a single mask. By visualizing axon correlation values and their fluorescence traces within the Suite2P GUI, we chose axon segments to merge based on correlation values and footprint distributions. Using custom Python code with functions from Suite2P’s source code, we ‘merged’ axons by generating new ROIs with these new pixels. The old axon segments were then eliminated from analysis and deconvolution was run on the new axon masks.

For all experiments, deconvolved signals were taken as the selected output from Suite2P and processed further in MATLAB 2021a. Deconvolved signals were smoothed by a rolling mean of 10 frames (0.32 seconds), then z-scored, and finally values below 2 were set to zero. The resulting signal was what was used for all analysis and referred to as ‘firing rate (STD)’ as a proxy for spiking activity. Signals were aligned to the trial structure (odor presentations, reward period, lick timing) and the recorded locomotion as mice ran on the spherical ball.

BTSP event detection and analysis

First, 6-second periods were extracted for each odor presentation period (2 seconds before odor and 3 seconds after) and divided for Odor A and Odor B regardless of whether it was the first or second odor presented in the trial. Since each recording had 5 blocks of 20 trials, we have 100 odor presentations of each odor per neuron per day. Next, we identified each 'event'; which we define as a group of consecutive timepoints with a non-zero deconvolved signal. The size and timing of that event is counted as the peak value within the event and that timepoint's time relative to the odor, respectively.

Next, we identified which events satisfied criteria to be considered as a possible induction event. This detection was performed separately for Odor A and Odor B presentations. Events in the first 10 or last 10 odor presentations were not considered for analysis, because we needed enough odor presentations before and after the event to detect BTSP events. There were two criteria for an event to be considered a possible induction event: during the previous 3 odor presentations the neuron must show no activity within 2 seconds before or after the event in question, and there must not have been a significant peak firing field. To determine the significance of a firing field, we took 6-second periods of all previous odor presentations and found the peak of the average activity. We then circularly shuffled each odor presentation and found the peak of the average activity from this shuffled data. This was repeated 2000 times to generate 2000 peak values from shuffled data. For a possible induction event, the real peak of average activity must not have been greater than the 90th percentile of the shuffle.

If an event passed criteria to be considered as a possible induction event, we analyzed if it was successful in forming a field. There were four criteria for a successful field formation: 1. The resulting field must have been significant above the 95th percentile of the shuffle; 2. The resulting field occurred within 2 seconds of the peak of the induction event; 3. The neuron must have fired (have value above 2 STD) within 0.5 seconds of the resulting field for the next 3 odor presentations; 4. The neuron must have fired within 0.5 seconds of the resulting field for at least 7 out of the next 10 odor presentations. All these criteria were decided by visually inspecting all successful events and improving based on our expectations of how BTSP events would look in our task. The strict criteria for activity in the previous 3, following 3, and following 10 odor presentations improves the likelihood that the event in question does induce the resulting field. The $\pm$ 2 second window for the difference between the event peak and field peak allowed us to look for asymmetrical formation without any bias. The lack of any criteria regarding the amplitude of the induction event allowed us to probe the relationship of amplitude to success rate and asymmetrical formation. Success rate increases continuously with amplitude (Figure 1 I), but only events with amplitude above 10 STD had statistically significant asymmetrical formation. Therefore, we considered any event above 10 STD to be 'plateau-like', and successful 'plateau-like' events are what we considered to be 'BTSP-like' events. We considered any event between 2 and 10 STD to be a 'small event'.

Locomotion analysis

1D locomotion that was recorded with a sensor (Avago ADNS-9500) at 1kHz was binned to match the frame rate of calcium imaging. Binned signals were smoothed by a rolling mean of 10 frames (0.32 seconds), then z-scored, and finally values below 1 were set to zero. These binned signals are displayed as 'locomotion (a.u.)'. Since most of the locomotion was small movements around the onset and offset of odors, in other analysis we binarized locomotion into 'not running' and 'running' bouts. A bout of running must have been at least 2 seconds of locomotion values above 1; and all other periods were considered to be 'not running'.

Selectivity analysis

We calculated the odor-selectivity index value for each ROI as: SI = $(R_a - R_b) / (R_a + R_b)$; where R_a is the firing rate at a given bin for Odor A trials and R_b is the same for Odor B trials. The same approach was taken for selectivity of match trials versus non-match trials. Bin sizes were always 0.5 seconds, and performance was never considered, so all trials are included. For each ROI, a distribution of 2000 shuffled index values were also calculated by randomly shuffling the trial type assignment 2000 times for each bin. The maximal absolute value index is chosen from all the bins (for the real ROI and all 2000 shuffles), and the bin is noted. ROI's with an absolute value index value above the 95th percentile of absolute value shuffled index values are considered to be 'significantly selective'.

Support vector machine decoding

Binary support vector machine (SVM) decoding was performed in MATLAB 2021a (default parameters) using bin sizes of 0.5 seconds (averaging the deconvolved signal for those frames within the bin). Unless otherwise noted, the number of ROIs was controlled by randomly subsampling 100 ROIs out of all possible ROIs. This 100 was chosen as it is the largest multiple of 50 that is smaller than the number of ROIs in each recording (CA1 and EC axons). In all cases, the result of 20 subsamples of ROIs were averaged for each data point. For each bin and subsample, 80% of trials were used for training the decoder, and the remaining 20% were used for testing. This was repeated 4 more times so that each block of 20 trials was used as the 20% for testing. For each training of the decoder, another training was done with a shuffled assignment of trial type to confirm a shuffle comparison of data yields decoder accuracy of $\sim$50%. For odor decoding, the trials were broken down into odor presentations (same as in BTSP detection analysis) to evaluate odor decoder accuracy regardless of the order of the odors. When specific timepoints were mentioned, such as 'during odor presentation' or 'during delay period', the average accuracies of the 0.5 second bins were averaged and not trained/tested with larger bins.

To evaluate the relationship of the number of subsampled ROIs and decoder accuracy, all the previous steps were repeated using different numbers of subsampled ROIs. Again 20 subsamples for each were used. If a recording session had fewer than the chosen number of ROIs, all ROIs were used. For axonal decoding in Figure S7 I-J we pooled axons from the different days of the same animal only in panels showing 'number of subsampled axons' on the x-axis. This was done simply to illustrate improved decoder performance with many more ROIs, but all other decoding figure panels were done by subsampling 100 axons and treating each recording session separately. For CA1 decoding in Figure S7 D, most recording sessions had more than 300 neurons, so no pooling of days was necessary.

Sequence-axon detection and analysis

To evaluate peak firing timing in EC axons, we performed sequence-axon detection similar to the previously described approach in CA1 neurons in our DNMS task, Taxidis et al. [18]. First, trials that begin with Odor A and those that begin with Odor B were separated, and the one with a larger peak of the average activity was considered further. Additionally, only the 6-second period including first odor presentation and the delay period was considered. In the same way as described in BTSP-event detection, the peak of average activity within this period and a given trial type was determined to be significant if the peak was greater than the 95th percentile of 2000 circular shuffles. The neuron must also have had a trial reliability of at least 20% (have fired above 2 STD for 20% of the preferred trials within 0.5 seconds of the peak frame found in the previous step). If an ROI passed both criteria, it was considered to be a 'sequence-axon' regardless of its odor-selectivity, as that was a separate analysis. An ROI was considered to have a peak during the odor presentation if the peak was within the odor presentation period. An ROI was considered to have a peak during the odor offset (sometimes referred

to as immediately after the odor) if the peak was in the first second of the delay period. An ROI was considered to have a peak during the delay period only if the peak was during the last 4 seconds of the seconds of the delay. This was done to not include the large population of ROIs that fired to the offset of the odor (likely the auditory cue of the clicking of the valve).

Analysis across days

For CA1 imaging, CellReg output registration maps were used to align cells across pairs. Within each pair saline and uPSEM days had the exact same cell indices. For decoding across days (Figure 4 C-D), the same binary SVM decoding was performed on subsamples of 100 neurons that overlap between the 2 days in question. Binning and all parameters were identical, with the exception that 100% of trials from the training day were used for training the decoder and 100% of trials from testing day were used for testing the decoder. To evaluate the percentage of overlapping neurons that remained odor selective (Figure 4 E), we used a threshold of the 90th percentile for odor-selectivity. If a neuron was found to have had a selectivity value above the 90th percentile and preferred the same odor in both days in question, then it was considered to 'remain odor selective'. All axonal analysis was performed separately for each recording session as alignment across days was difficult to achieve for each animal.

Statistical analysis

For CA1 imaging figures that show paired points, a single line connects the two days within a pair, so there are 4 times as many lines as animals. However, all statistics were performed as a Two-Way ANOVA (animal x pair) with repeated measures on the saline-uPSEM condition (using 'fitrm' and 'ranova' functions in MATLAB 2021a), so as not to treat each pair as entirely independent. For non-paired points (Figure 4 D-E), Two-Way ANOVA (animal x pair) were performed. For when CA1 imaging groups were not compared (Figure 1 I-L), all 17 animals were treated independently, and statistics were one-sample t-tests (Figure 1 K). The Wilcoxon signed-rank test was conducted using pairings of all neurons in CA1 recordings to evaluate the change of the distribution of selectivity values.

For axonal imaging figures, significance was determined on each day by two-sample t-tests for each day. ANOVA p-values are reported in the text as the overall significance using a Two-Way ANOVA (animal and day). For correlations with performance, Pearson's R was calculated with its corresponding p-value.

For all figures, no asterisks were shown if $p \geq 0.05$, 1 asterisk if $p < 0.05$, 2 asterisks if $p < 0.01$, 3 asterisks if $p < 0.001$. If the $p \geq 0.1$, 'n.s.' is displayed, but if $0.05 \leq p < 0.1$ the p-value was typically displayed in the figure. On occasions when single asterisks were displayed above a curve or trace, p-values were corrected for multiple comparisons using the false discovery rate Benjamini-Hochberg procedure. In all cases in the text, values were written in the format 'mean $\pm$ standard deviation' (STD), while error bars in all figures show the mean and standard error of the mean (SEM). No statistical methods were used to determine appropriate sample sizes but were chosen as being comparable to sizes used in similar publications.